Journal of Magnetism and Magnetic Materials 513 (2020) 167104

Contents lists available at ScienceDirect

Journal of Magnetism and Magnetic Materials

journal homepage: www.elsevier.com/locate/jmmm

Research articles

Magnetoimpedance, Jahn-Teller transitions upon electron doping of manganese sulfide

S.S. Aplesnin[a,b], M.N. Sitnikov[a], A.M. Kharkov[a,*], S.O. Konovalov[a], A.M. Vorotinov[b]

[a] Reshetnev Siberian State University of Science and Technology, 660037 Krasnoyarsk, Russia
[b] Kirensky Institute of Physics, Federal Research Center KSC SB RAS, Akademgorodok, 50, 660036 Krasnoyarsk, Russia

ARTICLE INFO

Keywords:
Impedance
Prehistory of magnetic susceptibility
Magnetoimpedance
Fermi glass
Orbital magnetic moment
Electron paramagnetic resonance
IR spectra
JT transitions
Conductivity

ABSTRACT

The effect of a magnetic field on the electrical and magnetic properties of manganese sulfide upon electron doping in the $Yb_xMn_{1-x}S$ ($0.05 < x < 0.2$) compound has been investigated. The change in the conductivity type from the Poole–Frenkel to Mott law have been established using the I–V characteristics and the change in the carrier type upon temperature and concentration variations has been observed. The effect of the sample prehistory on the conductivity, impedance, and magnetic susceptibility under the action of a magnetic field in a wide temperature range has been found. The trivalent state of ytterbium ions has been determined using the electron paramagnetic resonance study. The dynamic JT transitions temperature are found by IR method and by the electron paramagnetic resonance. Anomalies of carrier mobility and magneto-impedance were found in the vicinity of the Jahn-Teller transitions. The experimental data are explained by the localization of electrons with the formation of the interstitial orbital momenta and an orbital momentum into the site. The sample prehistory is related to the lifting of the orbital angular moments degeneracy and the direction of the axis of distortion of the octahedrons in a magnetic field.

1. Introduction

The creation of new materials with the multiferroic properties [1–4] and conducting channels controlled by weak magnetic and electric fields [5–7] is of great importance for data recording and processing. The highly degenerate electron glasses characterized by the memory effect can serve, depending on the sample prehistory, as prototypes of neural network models [8] and memristor devices [9,10]. In semiconductors with a random potential, electrons are localized in potential wells, with quantized energy values. The electron density of states at the Fermi level is nonzero and the Fermi level lies below the mobility threshold. The localization of electrons can be described in the Fermi glass model, when there is a threshold (boundary) for the mobility of current carriers and the Mott law $\sigma = \sigma_0/\exp(T^*/T)^{1/4}$ at low temperatures [11]. In the case of the Anderson localization caused by disorder in the system, the electronic spectrum of excitations is continuous, the system is stable with respect to external excitations, and the mobility threshold is continuously shifted by external forces. A change in the degree of localization from strong to weak can be varied due to the concentration of doping of electrons. For example, the substitution of cations by ions of variable valency under the influence of chemical pressure can change the valence of the ion and the degree of doping of the semiconductor. A Fermi glass [12] can be obtained using electron and hole doping of disordered semiconductors based on the $Yb_xMn_{1-x}S$ chalcogenide compounds. The ytterbium ion exhibits the properties of variable-valence ions [13,14]. The molar volume of divalent YbS is 27 см^3/mol, trivalent 24 cm^3/mol. A decrease in the elastic stresses in $Yb_xMn_{1-x}S$ upon substitution of manganese with ytterbium is possible due to the transition of the electron from $4f^{14}$ to the 5d level and partial delocalization of the electron in the Mn-Yb-Mn cluster.

Upon substitution of ytterbium ions for manganese cations, the pressure of the nearest environment will change the valence of ytterbium ions and lead to the formation of a metallic bond, as was observed in the YbS compounds under pressure. Under normal pressure, ytterbium sulfide is a semiconductor with a direct gap of ~1.3 eV in the electron excitation spectrum and an indirect gap of ~1.0 eV between the fully occupied 4f state and the empty sd band states [15], which are located higher than the 3p valence band of sulfur ions by 4 eV. Under the action of pressure, the gap monotonically narrows according to the relation $dE_g/dp = -6 \pm 1$ eV/kbar [16] and, at P = 8 GPa, the bands overlap and the metallic state occurs [17].

The substitution of ytterbium for manganese will shift the f level. Here, different scenarios can be observed. The f level lie in the

* Corresponding author.
E-mail address: khark.anton@mail.ru (A.M. Kharkov).

https://doi.org/10.1016/j.jmmm.2020.167104
Received 12 April 2020; Received in revised form 1 June 2020; Accepted 3 June 2020
Available online 05 June 2020

conduction band and the electron passes from the f to d level of the rare-earth ion or remains below the conduction band, being still bound with the donor. If the concentration of such centers is low (below the critical concentration of the impurity band formation of the percolation threshold), then the compound remains a semiconductor. The transition of an electron from the f level to the t_{2g} state will lead to the electron degeneracy, which can be lifted by the spin–orbit or Jahn–Teller interaction. The possible formation of the orbital ordering of electrons on the t_{2g} orbitals was investigated using a three-band model in the dynamic molecular field approximation [18]. The Coulomb potential parameters, the electron filling concentration corresponding to the Mott transitions, and different types of the orbital ordering, including those in the incommensurate structures, were found [18–20]. At certain parameters of the Hund exchange and Coulomb potential, the orbital ordering, which exists above the Curie temperature, causes the magnetoresistive effect in the absence of spin ordering [21]. At the higher dopant concentrations, the orbitally disordered state with orbital polarons can occur in the high-temperature region [22]. The shape of orbital polarons depends on the configuration of electronic orbitals and can take a disk or chain shape, depending on the ratio between the pseudo-orbital momenta and hopping integrals. In a magnetic field, with account for the phase of electron, the energy of the disk-shaped orbital polaron will be lower than the energy of the chain-shaped one. In the absence of static lattice deformations, this can induce the magnetoresistive effect.

The aim of this study is to determine the spin state of ytterbium ions, establish the memory effect on the transport and magnetic characteristics after the action of a magnetic field, elucidate the existence of Jahn-Teller transitions, and find the glass state with the random distribution of orbital angular momentum.

2. Experimental results and discussion

The syntheses of the $Re_xMn_{1-x}S$ samples was described in [23]. The X-ray diffraction analysis of the $Yb_xMn_{1-x}S$ sulfides was made on a DRON-3 X-ray diffractometer (CuKα radiation) at a temperature of 300 K after the synthesis and the measurements. The X-ray diffraction patterns of the initial $Yb_xMn_{1-x}S$ solid solutions contain, along with the diffraction reflections of the NaCl-type cubic structure, very weak reflections of impurity phases that may be attributed to rhombic phase (Fig. 1). The main [2 0 0] peak splits into two peaks (Fig. 1b) for x = 0.15, 0.2 with $2\Delta\theta = 0.33$ and 0.38. Possible it is a Jahn-Teller (JT) effect, reflecting an electronic instability associated with antiphase along -z ions motion which modulate bond length along the x and y directions (Fig. 1a). This leads to a doubling of the unit cell [24]. With an increase in the concentration, the unit cell parameter linearly increases. It was established that heating of the $Yb_xMn_{1-x}S$ system up to a temperature of 500 K during the impedance measurements did not significantly affect the crystal structure: all the reflections of both the main NaCl-type phase and the impurity phase remained. However, the intensity of the reflections in the X-ray diffraction patterns was redistributed.

The substitution of Yb^{2+} ions with the empty 4 d shell for two-valence manganese ions is equivalent to the hole doping and the substitution of trivalent ytterbium ions will lead to the electron doping with the formation of the space-charge regions, which was observed in manganites [25,26]. This model is confirmed by the electrical measurements.

3. I–V characteristics and hall measurements

We establish the conductivity mechanism from the *I–V* characteristics measured by the compensation four probe method on direct current in the temperature range of 80–400 K. The voltage dependence of the current in semiconductors can be described by the Ohm's law and the power and exponential functions. At low concentrations, the experimental *I–V* characteristics in the logarithmic coordinates are described by the Poole–Frenkel law (Fig. 2a), according to which a strong electric field applied to the sample changes the form of potential barriers for carriers between the crystal lattice atoms. This leads to an increase in the number of electrons in the sample due to overcoming the potential barrier. In this case, the current exponentially depends on the voltage [27]:

$$I = e\mu\eta_0 \frac{U}{L} \exp \frac{\beta U^{1/2}}{kTL^{1/2}} \quad (1)$$

where e is the elementary charge, μ is the mobility of carriers, n_o is the electron density in the conduction band in zero field, U is the applied voltage, k is the Boltzmann constant, and β is the Poole–Frenkel constant depending on semiconductor permittivity ε.

The linear dependence of I/U on $U^{1/2}$ in the logarithmic coordinates allows us to assume that the dominant carrier transport is associated by the hopping conductivity and tunnel emission of electrons [27]. In the $Yb_xMn_{1-x}S$ (x = 0.15, 0.2) solid solutions, the Mott conductivity prevails in the percolation concentration range (Fig. 2b, c). In the semiconductors with the charge ordering, the conductivity is described in the framework of the model of space-charge-limited currents [28]:

$$I = \frac{9}{8}\tau_\mu \sigma_0 \mu \frac{U^2}{L^3} S \quad (2)$$

where S is the sample area, τ_μ is the Maxwell relaxation time, σ_0 is the electrical conductivity in the bulk of the material, μ is the carrier mobility, and L is the sample thickness.

It was found that the magnetic field does not affect the conductivity mechanism. In a magnetic field, the electrical conductivity changes by no more than one percent.

The temperature conductivity of $Yb_xMn_{1-x}S$ samples is shown in Fig. 3. For a concentration of x = 0.05 in the temperature range

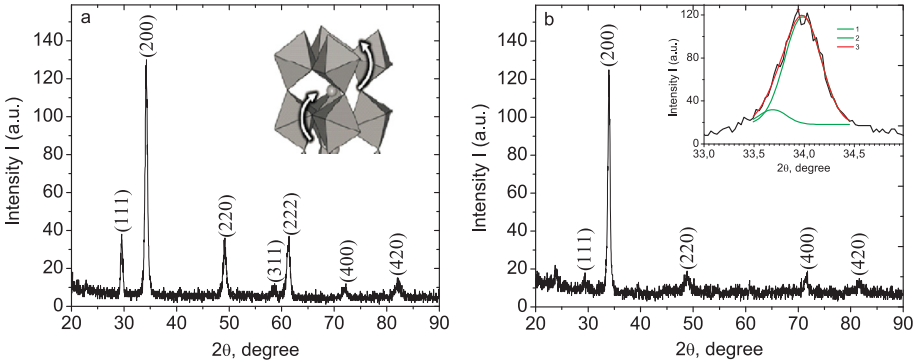

Fig. 1. X-ray diffraction pattern of the $Yb_{0.05}Mn_{0.95}S$ (a) and $Yb_{0.15}Mn_{0.85}S$ (b) samples at room temperature. Insert: rotation of octahedrons in anti-phase along -z (Fig. 1a). Insert: the main [2 0 0] peak splits into two peaks (1,2) for x = 0.15, peak sum (3) (Fig. 1b).

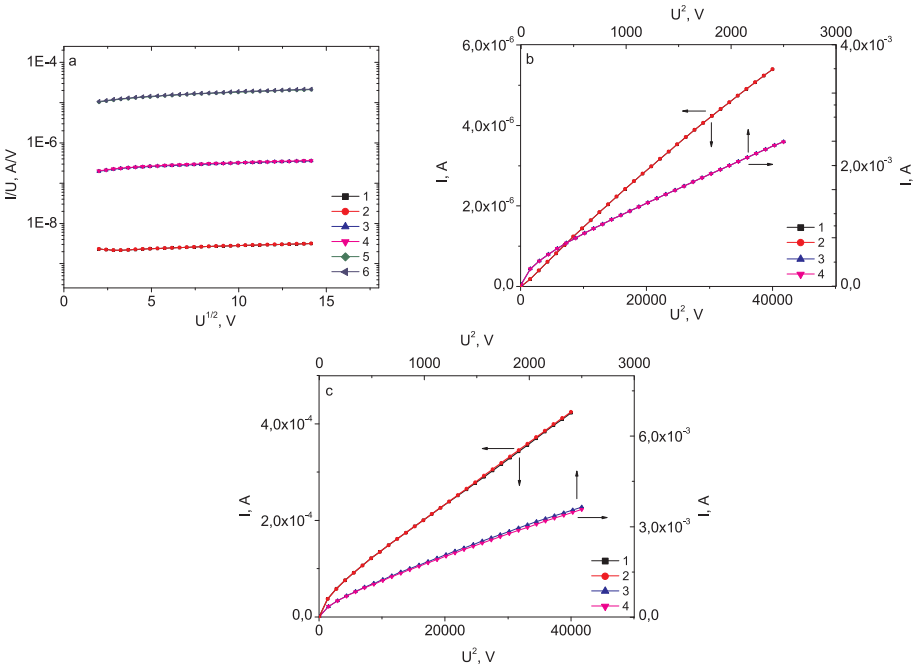

Fig. 2. (a) – Logarithmic dependence of I/U on $U^{1/2}$ for the sample $Yb_xMn_{1-x}S$ with x = 0.05 without a field at T = 120 K (1), 200 K (3), 320 K (5) and a magnetic field H = 12 kOe at T = 120 K (2), 200 K (4), 320 K (6). (b, c) – Current from the applied voltage U^2 for the sample $Yb_xMn_{1-x}S$ with x = 0.15 (b) without a field (1,3) at T = 160 K (1), 360 K (3) and the magnetic field H = 12 kOe at T = 160 K (2), 360 K (4) and for x = 0.2 (c) without a field at T = 240 K (1), 360 K (3) and magnetic field H = 12 kOe at T = 240 K (2), 360 K (4). X – axis voltage $U^{1/2}$ and U^2.

205–230 K, a crossover of conductivity is observed from the hopping mechanism described by the function $\sigma = \sigma_0/\exp(\Delta E/T)$ to the conductivity with a variable jump length with $\sigma = \sigma_0/\exp(T^*/T)^{1/4}$, which indicates the formation of Fermi glass. With an increase in the concentration of ytterbium ions, the deviation of the conductivity from (1/T) shifts to low temperatures at T = 124 K with x = 0.15 and is absent for the concentration x = 0.2 (Fig. 3). The activation energy in the sample decreases with increasing concentration from $\Delta E = 0.37$ eV with x = 0.05 to $\Delta E = 0.19$–21 eV with x = 0.15, 0.2 in the range of 200–350 K. The kink in σ (T) in the range 445–460 K is associated with the localization of electrons in the vicinity of ytterbium ions, which leads to the formation of random electric fields of charged centers. This can be described in a model with random potential V. If the potential electron energy is $V \gg W$ (W is the dispersion width of the potential wells), then this will lead to the localization of the electron described in the Anderson model. In the Anderson's insulator, the density of states at the Fermi level is finite. As a result of thermal fluctuations, electrons or holes move to the mobility edge and participate in diffusion conductivity (which will be determined below from the impedance hodograph), and holes or electrons located below the mobility edge

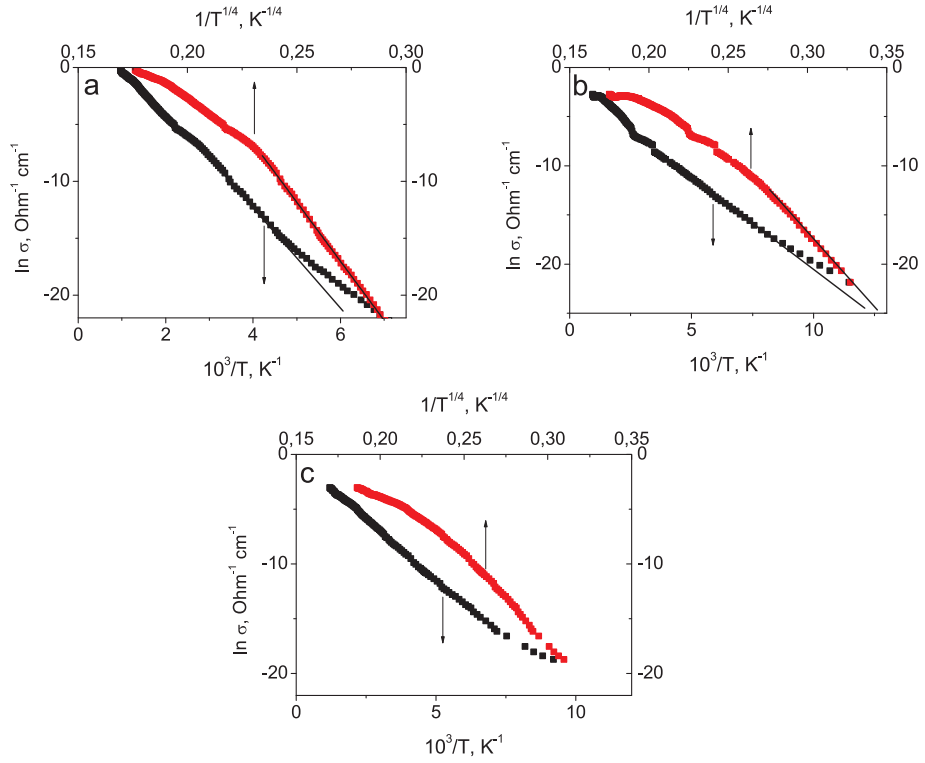

Fig. 3. Conductivity of the sample $Yb_xMn_{1-x}S$ with x = 0.05 (a), 0.15 (b), 0.2 (c) versus the inverse temperature and of $1/T^{1/4}$.

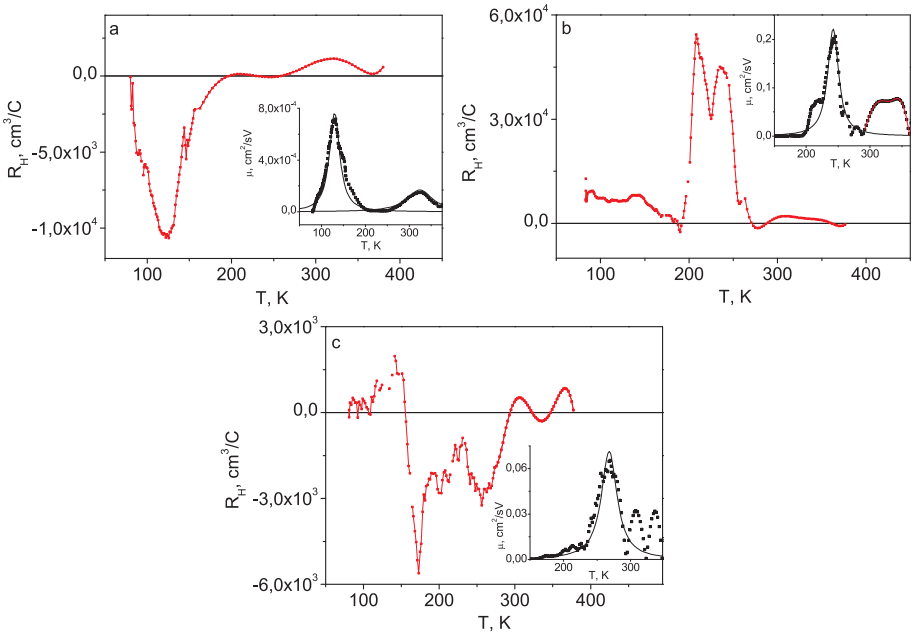

Fig. 4. The temperature dependence of the Hall coefficient measured in the magnetic field H = 12 kOe perpendicular to the current for the samples $Yb_xMn_{1-x}S$ with x = 0.05 (a), 0.15 (b), 0.2 (c). Inserts: mobility of carriers versus temperature: experiment (dots), fitting function (3).

contribute to the hopping conductivity.

The change in the conductivity mechanism upon concentration is consistent with the change in the carrier sign. Fig. 4 shows the Hall constant in a magnetic field of 12 kOe. We extract the prevailing the type hole and electron current carriers using the $R_H(T)$ dependence. Below 200 K, the conductivity of the $Yb_xMn_{1-x}S$ (x = 0.05) compound is due to electrons. Above 200 K, the holes contribution to the conductivity dominates. In the solid solution with x = 0.15 the current is associated with holes and for x = 0.2 due to electrons in the temperature range of 150–300 K. The conduction and valence band boundaries give rise to the tales of the density of states, which are overlap. The tales of the valence and conduction bands form the donor and acceptor states with a random Coulomb field. In manganese sulfide, a distortion of the structure from cubic to rhombohedral at T_2 = 165 K and compression of the lattice at T_1 = 125 K were found [29]. Structural transitions induce a blue shift of the edge of the absorption band [30] and cause a shift of the chemical potential. The chemical potential shifts to the region of donor electronic states upon heating of $Yb_xMn_{1-x}S$ (x = 0.05), and the temperature of the mobility maximum at T = 130 K (Fig. 4a) determined in the single-band model $\mu = R_H/R$ (R is the sample resistance, R_H is Hall constant), is in the temperature region of the lattice deformation.

A change in the symmetry in $Yb_xMn_{1-x}S$ for $x < x_c = 0.17$ (x_c is the concentration of ytterbium ions in the fcc lattice) at T_2 = 165 K shifts the conduction band and chemical potential to the region of acceptor states upon heating. The mobility $\mu = e\tau/m_{ef}$ depends on the effective mass m_{ef} and the relaxation time τ. Deformation and local distortions of the octahedra can occur as a result of lifting the triple degeneracy of the t_{2g} level (Jann-Teller effect). A change in the mobility of current carriers will be caused by a strong electron-lattice interaction. In the model of phase transitions, the relaxation time is determined by the correlation radius and has the form $\tau = \tau_0/(1 - T/T_c)^{z\nu}$ (z,ν are critical indices). The dispersion in the distribution function of the random potential will lead to a different of critical temperatures $T_c \pm \Delta T$. We approximate the temperature dependence of mobility by the function:

$$\mu = \frac{A}{\left(1 - \frac{T}{T_c}\right)^{z\nu} + \Delta T^2} \quad (3)$$

where $z\nu = 2$ gives the minimum error of fitting function (3) to the experimental results (Fig. 4). From the values of the critical indices, one can estimate the degree of disorder in the system. In the disordered Ising model with nonmagnetic impurities and with interactions between the nearest neighbors with a weak disorder $z\nu = 1.4$, with a strong disorder $z\nu = 1.9–2.1$ [31–33]. Critical temperatures are presented in Table 1.

The mobility of holes is several times greater than the mobility of electrons. The density of electronic states at the chemical potential is an order of magnitude higher than the density of holes in the range 160–300 K, which indicates the localization of electrons.

4. Impedance spectroscopy

The temperatures of local distortions of the structure, accompanied by charge fluctuations, and the influence of the prehistory on the topology of potential wells with localized electrons under the influence of a magnetic field are determined from the impedance and ac resistance. Fig. 5 presents the active and reactive parts of the impedance and Z(T) vs reciprocal of temperature for the composition with x = 0.05. One can see two impedance jumps at T = 124 K and at T = 156 K, that associated with structural deformation of lattice (insert in Fig. 5b) [29]. A small R(T) maximum at T = 468 K is frequency-independent and results from the carrier scattering by structural deformations induced ytterbium ions. The plateau-like region in Z (T) in the range 370–420 K gradually narrows and disappears at a frequency of ω = 300 kHz. The electric field created by Yb^{3+} ions is partially compensated by impurity current carriers. Induced local electric polarization depends on the topology of the electron density distribution in the cluster of Mn-Yb-Mn and JT transitions.

(b) – The dependence of the impedance Z on the inverse temperature 1/T for the sample $Yb_xMn_{1-x}S$ with x = 0.05, measured in a zero

Table 1
Critical temperatures phase transitions of strong disordered systems.

x	T_{1c}, K	ΔT_1	T_{2c}, K	ΔT_2	T_{3c}, K	ΔT_3
0.05	130	12	325	35	–	–
0.15	245	10	315	12	344	9
0.2	266	14	308	7	337	6

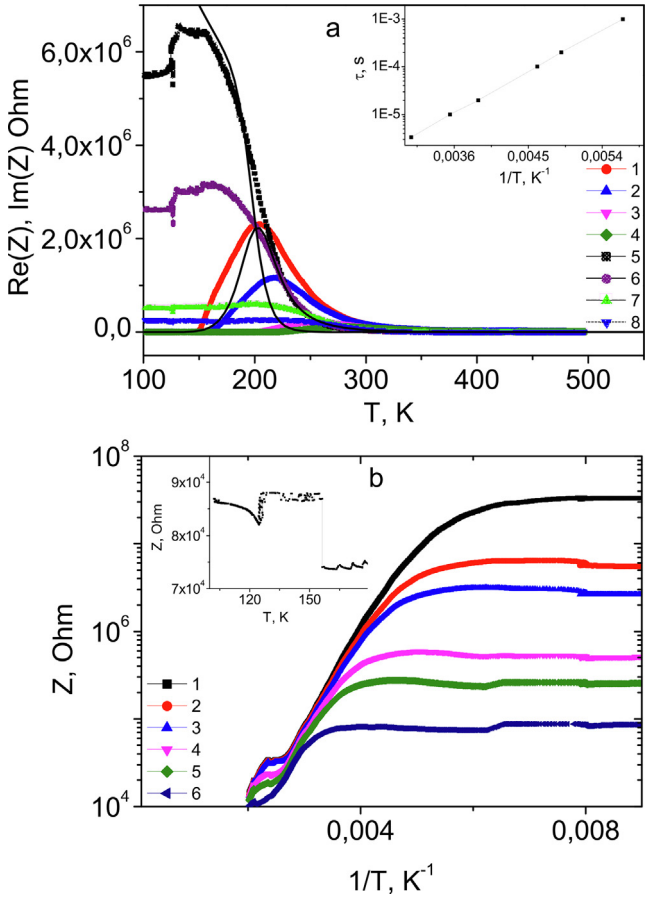

Fig. 5. (a) – Temperature dependences of real Re(Z) and imaginary Im(Z) parts of impedance for the sample $Yb_xMn_{1-x}S$ with x = 0.05, measured in zero magnetic field for Re(Z) at frequencies ω = 5 kHz (1), 10 kHz (2), 50 kHz (3), 100 kHz (4) and for Im(Z) at frequencies ω = 5 kHz (5), 10 kHz (6), 50 kHz (7), 100 kHz (8). Theoretical calculations of the impedance by formula (4) are solid lines. Insert: Dependence of the relaxation time τ on inverse temperature 1/T.

magnetic field at frequencies ω = 1 kHz (1), 5 kHz (2), 10 kHz (3), 50 kHz (4), 100 kHz (5), 300 kHz (6). Insert: Z(T) at frequency ω = 300 kHz.

The ac conductivity exhibits the resistance maxima at temperatures that depend on frequency (Fig. 5a). The relaxation time for this polarization mechanism can be determined from the impedance components using the Debye model:

$$ReZ(\omega) = \frac{A}{1+(\omega\tau)^2} \quad ImZ(\omega) = \frac{A\omega\tau}{1+(\omega\tau)^2} \tag{4}$$

where the relaxation time τ obeys the Arrhenius law $\tau = \tau_0 \exp(\Delta E/kT)$ with ΔE = 0.19 eV and τ_0 = 3 GHz. In the Debye model, the relaxation time is found from the relation τ = 1/ω and the maximum temperature Im (Z) at a given frequency. The insert in Fig. 5a shows the logarithmic dependence of the relaxation time on inverse temperature. The impedance exhibits the activation dependence $Z = Z_0\exp(\Delta E/kT)$ in the temperature range of 240–350 K with an activation energy of ΔE = 0.218 eV. At low temperatures, the reactive part of the impedance decreases according to the power law Im(Z(T = 100 K))/Im(Z(T = 400 K)) = ω_c/ω, where $\omega_c = 4{\cdot}10^6$ Hz.

In the $Yb_xMn_{1-x}S$ (x = 0.15) compound (Fig. 6), the imaginary part of the impedance Im(Z(T)) has two inflection points and the real part Re (Z(T)) has two maxima. The temperature dependence of the impedance components is described using the Debye model with two relaxation times:

$$ReZ(\omega) = \frac{A}{1+(\omega\tau_1)^2} + \frac{B}{1+(\omega\tau_2)^2}, \quad ImZ(\omega) = \frac{A\omega\tau_1}{1+(\omega\tau_1)^2} + \frac{B\omega\tau_2}{1+(\omega\tau_2)^2} \tag{5}$$

where $\tau_{1,2} = \tau_{01,2}\cdot\exp(\Delta E_{1,2}/kT)$ with activation energies of ΔE_1 = 0.17 eV and ΔE_2 = 0.37 eV. The two relaxation channels are associated with two переходами, in which the triple degenerate t_{2g} state is successively lifted. The asymptotic continuation of Im(Z (T = 100 K))/Im(Z(T = 400 K)) upon frequency yields a critical frequency of $\omega_c = 2{\cdot}10^7$ Hz above which the impedance anomalies below 400 K vanish. If the frequency of the external electromagnetic field exceeds the frequency ω_c of the electron relaxation, then the local electric polarization is not varied. Heating in a magnetic field of H = 12 kOe reduces the ΔE_1 value from 0.17 eV at H = 0 to 0.16 eV at H = 12 kOe and increase the ΔE_2 value by 0.015 eV. The reactive part of the impedance consists of the inductive (L) and capacitive (C) contribution Im (Z) = Lω–1/ωC. The impedance Z (ω) is well described by the function $Z(\omega) = A/\omega^n$ with n = 1 at T < 300 K, and at higher temperatures n < 1. A decrease in the impedance in the magnetic field is caused by an increase in capacitance, and an increase in the impedance is associated with the inductive contribution current carriers. The corresponding impedance variations in a magnetic field (Z(H)–Z (0))/Z(0)) are shown in the inset in Fig. 6. In the temperature range of 148–240 K the impedance decreases in a magnetic field from 20% to 15% and from 45% to 14% at temperatures 460–490 K with an increase in the frequency from ω = 1 kHz to 300 kHz. An increase in the dZ/Z value by up to 50% in a magnetic field in the range of 300–412 K is caused by induction.

Above the percolation concentration, at x = 0.2, the ac resistance maximum is also observed in the range of 160–240 K (Fig. 7); the temperature of this maximum shifts to the low-temperature region in a magnetic field. The real and imaginary parts of the impedance are described in the framework of the Debye model. The functional dependence of relaxation time is described by the Arrhenius law with an activation energy of ΔE_1 = 0.2 eV at H = 0 and ΔE_2 = 0.19 eV at H = 12 kOe (insert in Fig. 7). The temperature dependence of the impedance has the activation character with ΔE = 0.2–0.22 eV; the activation energy decreases with increasing frequency. In a magnetic field, the impedance decreases from 40% at ω = 1 kHz to 25% at ω = 300 kHz at temperatures of 191–275 K. In the temperature range 290–340 K, where mobility has a maximum, the impedance in the magnetic field decreases from 20% to 0 in the frequency range 1–50 kHz. The maximum values of magneto-impedance are achieved at low frequencies in the vicinity of JT junctions.

We determine the effect of the external magnetic field on the impedance with and without magnetic field at fixed temperatures. In the temperature range of 80–250 K, the frequency dependence of the impedance is described by the power function Z = A/ω; i.e., the impedance is determined by the capacitance and its change in the magnetic field is no larger than 1%. The impedance hodograph is described by a parallel RC contour in the equivalent circuit model (Fig. 8). At 200 K, the reactive part of the impedance is extended in a tilted ellipse due to adding the diffusion contribution (insert in Fig. 8).

The impedance hodograph in the $Yb_xMn_{1-x}S$ (x = 0.15) compound can be described in the model of equivalent circuits in the form of an RC contour at high frequencies (Fig. 9) and by the linear dependence at low frequencies (insert in Fig. 9). The semi-circumference center lies below the Re(Z) axis and is marked by an element of the constant phase difference, which corresponds to the nonuniform distribution of the microscopic properties over a sample. Under the action of an ac current, the diffusion layer is formed in a sample, which is described by the Warburg impedance [34]:

$$Z_W(j\omega) = \lambda(j\omega)^{-\frac{1}{2}} = \lambda\omega^{-\frac{1}{2}}(1-j) \tag{6}$$

where λ is the Warburg coefficient, which is inversely proportional to

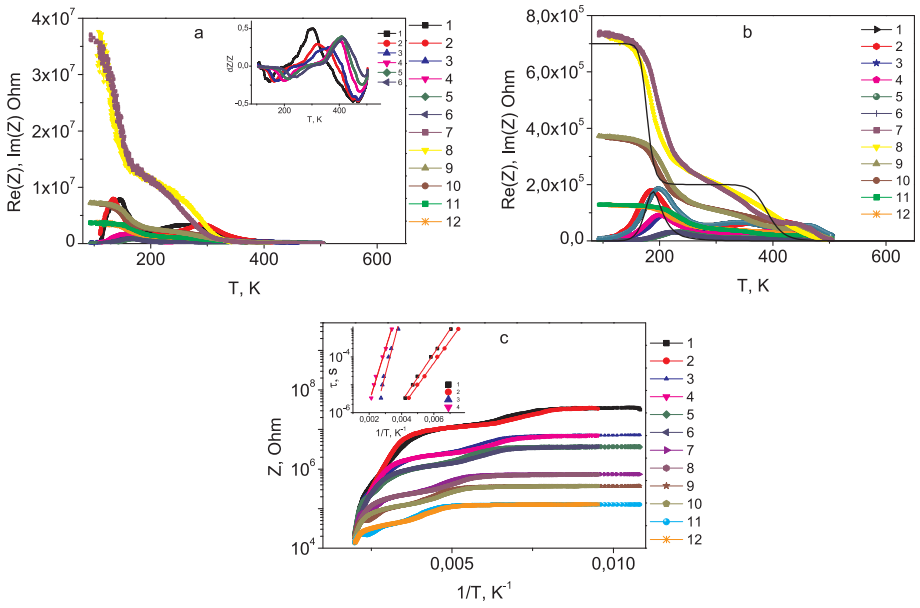

Fig. 6. (a) – Temperature dependences of real Re(Z) and imaginary Im(Z) parts of impedance for the sample $Yb_xMn_{1-x}S$ with x = 0.15, measured without field (1,3,5) and in magnetic field H = 12 kOe (2,4,6) for Re(Z) at frequencies ω = 1 kHz (1,2), 5 kHz (3,4), 10 kHz (5,6), and for Im(Z) at frequencies ω = 1 kHz (7,8), 5 kHz (9,10), 10 kHz (11,12) at H = 12 kOe (8,10,12). Insert: Temperature dependence of the magnetoimpedance (Z(H)–Z(0))/Z(0) at frequencies ω = 1 kHz (1), 5 kHz (2), 10 kHz (3), 50 kHz (4), 100 kHz (5), 300 kHz (6). (b) – Temperature dependences of real Re(Z) and imaginary Im(Z) parts of impedance Z for x = 0.15, measured without field (1,3,5) and in magnetic field H = 12 kOe (2,4,6) for Re(Z) at frequencies ω = 50 kHz (1,2), 100 kHz (3,4), 300 kHz (5,6), and for Im(Z) at frequencies ω = 50 kHz (7,8), 100 kHz (9,10), 300 kHz (11,12) at H = 12 kOe (8,10,12). Impedance calculations by expression (5) is plotted by solid lines. (c) – Dependence of impedance on the inverse temperature 1/T for the sample $Yb_xMn_{1-x}S$ with x = 0.15, measured without a field (1,3,5,7,9,11) and in a magnetic field H = 12 kOe (2,4,6,8,10,12) at frequencies ω = 1 kHz (1,2), 5 kHz (3,4), 10 kHz (5,6), 50 kHz (7,8), 100 kHz (9,10), 300 kHz (11,12). Insert: Dependence of the relaxation time τ with activation energies ΔE_1 = 0.17 eV (1,2), ΔE_2 = 0.37 eV (3,4) in magnetic field H = 12 kOe (2,4) on inverse temperature 1/T.

the diffusivity of the wave of charge density D: λ = k/D. The absolute value of the impedance decreases with increasing frequency. In the equivalent circuit model, it is denoted by symbol W and suggests the series connection of the resistance and capacitance, which depend on frequency ω [35].

At 450 K, the hodograph can be presented in the form of two RC chains connected in series (Fig. 9b) with the similar constant times $\tau_1 = R_BC_B$ and $\tau_2 = R_VC_V$ and the overlap of the semi-circumferences. Up to room temperature, the impedance spectrum is magnetic field-independent. Upon heating above 350 K, the impedance increases in a magnetic field and below 350 K the magnetoimpedance depends on the sample prehistory. The impedance hodograph contains a diffusion component in the low-frequency region in the temperature range of 160–350 K.

Above the percolation concentration for x = 0.2, the hodograph is described by the series connection of the RC contour and the diffusion component over the entire temperature range at frequencies of ω < 10^5 Hz. In the magnetically ordered region, the impedance grows in a magnetic field (Fig. 10). The impedance growth is attributed to a decrease in the capacitance in a magnetic field due to the redistribution of carriers over the antiferromagnetic sublattices as a result of the spin–orbit interaction.

The relaxation time found from Re(Z)(ω) and Im(Z)(ω) described by the Arrhenius law with an activation energy of ΔE_1 = 0.19 eV. The main contribution to the Z(ω) dependence is made by the capacitance below room temperature.

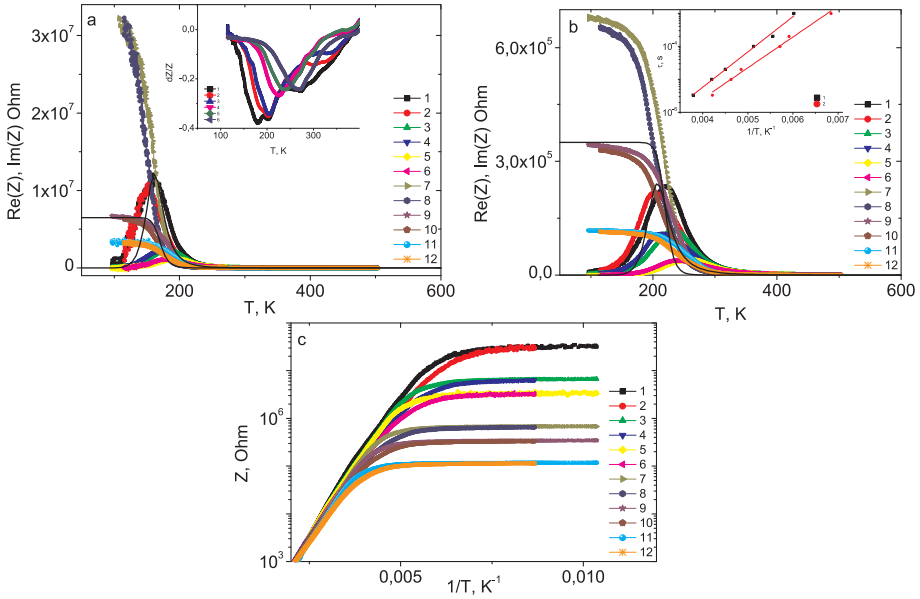

Fig. 7. (a) – Temperature dependences of the real Re (Z) and imaginary Im (Z) parts of the impedance for the sample $Yb_xMn_{1-x}S$ with x = 0.2, measured without a field (1,3,5) and in magnetic field 12 kOe (2,4,6) for Re (Z) at frequencies ω = 1 kHz (1,2), 5 kHz (3,4), 10 kHz (5,6), and for Im (Z) at frequencies ω = 1 kHz (7,8), 5 kHz (9,10), 10 kHz (11,12) at H = 12 kOe (8,10,12). Insert: Temperature dependence of the magnetic impedance (Z(H)–Z(0))/Z(0) at ω = 1 kHz (1), 5 kHz (2), 10 kHz (3), 50 kHz (4), 100 kHz (5), 300 kHz (6). (b) – Temperature dependences of the real Re(Z) and imaginary Im(Z) parts of the impedance for x = 0.2, measured without field (1,3,5) and in magnetic field 12 kOe (2,4,6) for Re(Z) at frequencies ω = 50 kHz (1,2), 100 kHz (3,4), 300 kHz (5,6), and for Im(Z) at frequencies ω = 50 kHz (7,8), 100 kHz (9,10), 300 kHz (11,12) at H = 12 kOe (8,10,12). Impedance calculations by expression (5) is plotted by solid lines. Insert: Dependence of the relaxation time τ without field (1), in magnetic field H = 12 kOe (2) on inverse temperature 1/T. (c) – Dependence of impedance on the inverse temperature 1/T for the sample $Yb_xMn_{1-x}S$ with x = 0.2, measured without field (1,3,5,7,9,11) and in magnetic field H = 12 kOe (2,4,6,8,10,12) at frequencies ω = 1 kHz (1,2), 5 kHz (3,4), 10 kHz (5,6), 50 kHz (7,8), 100 kHz (9,10), 300 kHz (11,12).

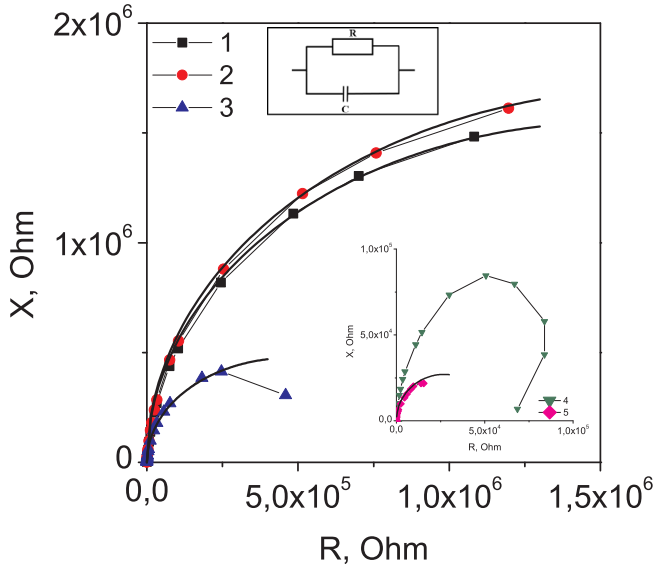

Fig. 8. Impedance hodographs in a zero magnetic field at T = 80 K (1), 120 K (2), 160 K (3) for the sample $Yb_xMn_{1-x}S$ with x = 0.05. Insert: Impedance hodographs in zero magnetic field at T = 200 K (4), 240 K (5).

5. Magnetic susceptibility and electron paramagnetic resonance

Lifting threefold electronic degeneracy in the t_{2g} subsystem will result in the appearance of an orbital angular momentum, that is reflected in the magnetic characteristics. The magnetic moment of the $Yb_xMn_{1-x}S$ solid solutions was measured in a magnetic field of 0.5 kOe upon heating and cooling in a magnetic field of 50 kOe. Fig. 11 shows the temperature dependence of the inverse magnetic susceptibility for the compositions with x = 0.05 and 0.15. Upon field cooling (FC), the magnetic susceptibility variation $(\chi_{FC} - \chi_{ZC})/\chi_{ZC}$ attains 1% at $T > T_{N(FC)}$ (inserts in Fig. 11). At x = 0.05, the susceptibility decreases by 0.5% and 0.85% in a magnetic field upon cooling in the ranges of 150–200 K and 220–270 K, respectively. This is caused by the diamagnetic contribution of the electrons localized in potential wells. In the model of free particles with the quadratic dispersion law, the equation of the diamagnetic susceptibility taking into account the difference between the carrier effective mass and electron mass was obtained [36]:

$$\chi_L = -\frac{4}{3}\frac{\gamma(\hbar\omega_H)^2}{2H^2} \quad \gamma = \frac{mp_F}{2\pi^2\hbar^3} \tag{7}$$

where ω_H is the distance between the Landau levels and m is the electron (hole) effective mass. Eq. (7) is valid at high temperatures ($T \gg \hbar\omega_H$). The Landau susceptibility is proportional to the density of states at the Fermi level. The typical diamagnetic susceptibility is 10^{-6} emu/mol [37]. The estimation of the diamagnetic susceptibility in the $Yb_xMn_{1-x}S$ compound from the temperature hysteresis yields 10^{-7} emu/mol and the electron effective mass is larger than the free electron mass by a factor of 5–7. The growth of the magnetic susceptibility at x = 0.15 upon cooling is consistent with an increase in the Hall constant in the range of 200–250 K. This effect is attributed to the diamagnetic contribution of holes with the negative effective mass. The contributions of electrons and holes can be determined from the electron paramagnetic resonance (EPR) spectra using the effective mass of carriers.

The $Yb_xMn_{1-x}S$ compositions with x = 0.05 and x = 0.15 were investigated using EPR in the temperature range of 100 K < T < 300 K. The EPR measurements were performed on a Bruker Elexsys E-580 spectrometer operating in the x range at a frequency of 100 kHz and an amplitude modulation of 1 Oe. For the composition with x = 0.05, the EPR line consists of two lines with g factors of 1.87 and 1.09 (Fig. 12). The sum of Lorentzian fitting lines coincide with experimental data. The substitution of ytterbium for manganese leads to a decrease in the g- factor of lines 1 and 4 for the $Yb_xMn_{1-x}S$ (x = 0.05) sample as compared with a value of g = 1.98 for MnS, which is caused by admixing of the electronic states with the orbital angular momenta. The applied magnetic field induces an additional magnetic orbital angular momentum and the orbital motion of an electron induces, in turn, the magnetic field directed oppositely to the applied field. The stronger the induced field, the weaker the local field on the spin system and the smaller the g factor. To obtain the resonance conditions, the external field strength should be higher, which corresponds to the negative deviation $-\Delta g$ from the purely spin value. Upon cooling, the g- factor of lines 1 and 4 smoothly decreases to 1.81 (Fig. 13). This is caused by the growth of the antiferromagnetic-type spin–spin correlations, which induce the local exchange field on manganese ions. The second line with g = 1.09 of lines 2 and 5 is caused by ytterbium ions with g = 8/7. Cooling to 150 K leads to a decrease in the g factor (g = 0.98) due to the exchange interaction of the spins of ytterbium and manganese ions. The EPR linewidth of lines 1 and 4 decreases upon heating and is approximated by a power dependence above the Neel temperature, which is indicative of the spin–spin mechanism of the magnetic moment relaxation (Fig. 14a). In the random phase approximation, the resonance linewidth in antiferromagnets changes according to the law $\Delta H = A/(T - T_N)^{1/4}$ with a decrease in temperature [37]. The experimental data are described well by a power dependence with an exponent of n = 0.28(4), T_N = 140 K at x = 0.05. The temperature dependence of the EPR signal intensity qualitatively coincides with the magnetic susceptibility $\chi(T)$ at x = 0.05.

As the concentration of the substitution of ytterbium ions for manganese ones increases, the g factor decreases to g = 1.7 of lines 3 and 4. The EPR resonance field on the Yb spins in the distorted octahedron grows and goes beyond the external magnetic field range. In fields of up to 7 kOe, the EPR spectrum consists of a single line 4 up to 200 K. Spin-orbit interaction leads to a splitting of the energy levels of localized ion spins in the Mn-Yb-Mn cluster, which causes resonance absorption of electromagnetic radiation in the microwave range (Fig. 12b) in a zero field. The absorption is asymmetric. When the spin polarization is lost, electrons generate microwave pulses with the coherent phases. This results in the interference, which can be either enhancing or weakening. Therefore, the power absorbed in different

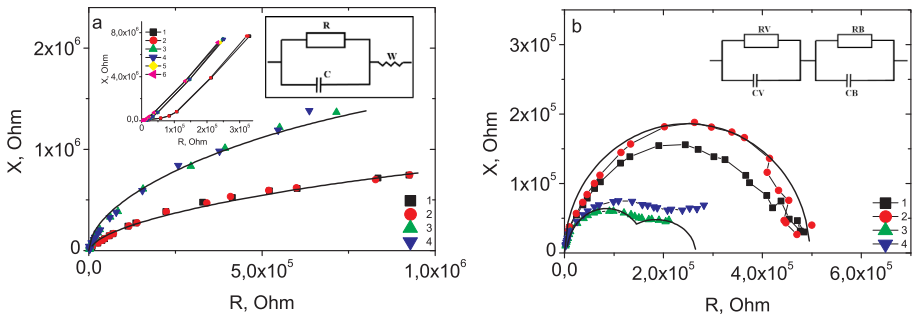

Fig. 9. (a) – Impedance hodographs in zero magnetic field (1,3) and in magnetic field H = 8 kOe (2,4) at T = 300 K (1,2), 350 K (3,4) for the sample $Yb_xMn_{1-x}S$ with x = 0.15. Insert: Impedance hodographs in zero magnetic field (1,3,5) and in magnetic field H = 8 kOe (2,4,6) at T = 200 K (1,2), 240 K (3,4), 280 K (5,6). (b) – Impedance hodographs in the zero magnetic field (1,3) and in the magnetic field H = 8 kOe (2,4) at T = 400 K (1,2), 450 K (3,4) for the sample $Yb_xMn_{1-x}S$ with x = 0.15.

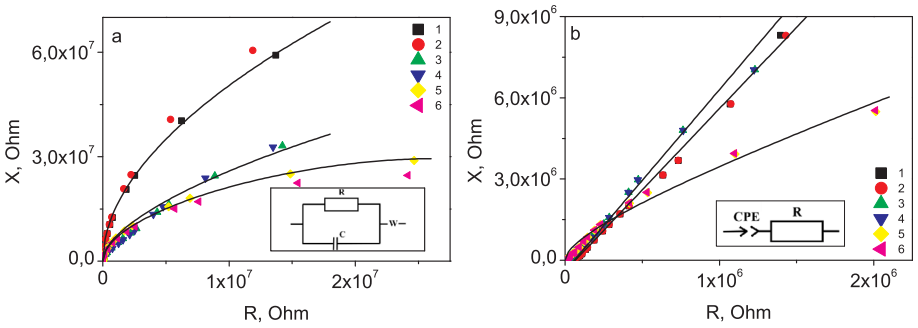

Fig. 10. (a) – Impedance hodographs in the zero magnetic field (1,3,5) and in the magnetic field H = 8 kOe (2,4,6) at T = 80 K (1,2), 120 K (3,4), 360 K (5,6) for the sample $Yb_xMn_{1-x}S$ with x = 0.2. (b) – Impedance hodographs in the zero magnetic field (1,3,5) and in the magnetic field H = 8 kOe (2,4,6) at T = 200 K (1,2), 240 K (3,4), 300 K (5,6) for the sample $Yb_xMn_{1-x}S$ with x = 0.2.

external magnetic fields can be lower than the power usually absorbed without field [37].

The averaged g factor in polycrystals with a magnetic field parallel to the trigonal crystal axis has the form $g_{av} = 2 - 8\lambda/\Delta E$ [38], where ΔE is the energy difference between the ground and excited states and λ is the spin–orbit interaction constant. The calculated g factor is consistent with an experimental value of g = 1.7 of lines 4 at parameters of $\lambda = 40\ cm^{-1}$ and $\Delta E = 960\ cm^{-1}$, which are determined using infrared (IR) spectroscopy. The deviation of the g factor from the value for a free spin is determined by the spin–orbit interaction (δ) and electron effective mass [39]:

$$g = 2 + \frac{\delta}{\Delta E}\left(\frac{m_0}{m} - 1\right) \quad (8)$$

Increase in mobility of holes below 270 K induces an additional orbital magnetic moment and a magnetic field, which shift the external magnetic field to the left and increase the g factor of line 4. The g(T) dependence (Fig. 13) correlates with the $R_H(T)$ behavior. The EPR linewidth has a small maximums at 200 K and 250 K associated with transfer of energy from spin system to elastic by spin-orbital interaction (Fig. 14b).

We find the asymmetry of the EPR line shape from the ratio between the maxima of the absorption line derivative $Y_1 = dP(H < H_r)/dH$ and $Y_2 = dP(H > H_r)/dH$ (Fig. 15). Upon approaching the Neel temperature, the asymmetry increases due to the enhancement of the spin–spin interactions with the ytterbium spins at x = 0.05. The ratio Y_1/Y_2 depends on the ratio between the spin diffusion time T_D and the spin relaxation time T_1. The maximum of the derivative of the ratio Y_1/Y_2 is obtained at $T_D = 0.2\ T_1$ [37]. Below 200 K, the spin diffusion time sharply decreases as compared with the spin relaxation time.

The IR absorption spectra are presented in Fig. 16a. In the frequency range of 900–1100 cm^{-1}, the $Yb_{0.15}Mn_{0.85}S$ compound demonstrates two absorption peaks at $\omega_1 = 953\ cm^{-1}$ and $\omega_2 = 994\ cm^{-1}$. Upon heating at T > 200 K, the first peak at frequency ω_1 vanishes and the intensity of the second peak decreases exponentially (insert in Fig. 16b). The frequencies shift upon heating by 3 and 12 cm^{-1}, respectively. The formation of two IR absorption lines is related to the spin–orbit interaction (about 40 cm^{-1}). IR absorption is associated with the Jan-Teller mode and the transition at 200 K from dynamic to static mode. The direction of distortion of the octahedra along the cube axes is three times degenerate with the height of the potential barrier E_b. The intensity of the transition between degenerate states is well described by the expression $I = I_0 \cdot \exp(E_b/kT)$ with $E_b = 0.1$ eV.

6. Model

The ionic radius of Yb^{3+} is 5% smaller than the radius of Yb^{2+}. Under the action of chemical pressure, especially in Mn-Yb-Mn clusters in which ytterbium ion is surrounded by manganese ions, a partial filling of the 5d shell is possible. In a cubic crystal with one electron on the t_{2g} shell, triple degeneracy occurs, which can be lifted by strong electron correlations, spin–orbit interaction, and anion displacement with a decrease in symmetry (Jahn-Teller effect). In the paramagnetic state, the spin–orbit interaction and the interorbital Coulomb interaction with one electron can be neglected. Threefold degeneracy of the electron in the t_{2g} shell below 360 K is lifted by the dynamic effect of JT, which determines the correlation of the motion of electrons with the motion of ligand nuclei. The energy JT characterizes the magnitude of the interaction between the electrons and the crystalline field arising from the deformation of the octahedron. The local crystal field in the $D\Gamma_5$ state can acquire the tetragonal, trigonal, or rhombic symmetry. The active distortions of the crystal lattice in the linear Jahn – Teller interaction are determined by tetragonal (E_g), rotational distortions (T_{1g}), and bending (T_{2g}) vibration modes of the octahedron. In perovskites with increasing temperature, a sequence of distortions T_{2g}, T_{1g}, and Eg is realized [40–42]. Perhaps in the range 325–350 K a dynamic JT transition occurs with T_{1g}, which pass into T_{2g} at 245–266 K. In the presence of vacancies or excess localized electrons, the dynamic effect of JT pass into a stable static local distortion, which is determined from the EPR. Threefold degeneracy occurs, corresponding to three possible choices of the axis of distortion of the octahedron. The spatial distribution of the electron density of the cation follows a change in the configuration of the ligands and the rotation of the electron cloud gives a large diamagnetic contribution to the susceptibility. The direction of the diamagnetic magnetization in the field is determined by the direction of the axis of distortion of the octahedron.

In the t_{2g} shell, we can separate the effective moment L = 1 with the eigenfunctions indexed by its projections ψ_0, $\psi_{\pm1} = \pm\frac{1}{\sqrt{2}}(d_{xz} \pm id_{yz})$. The

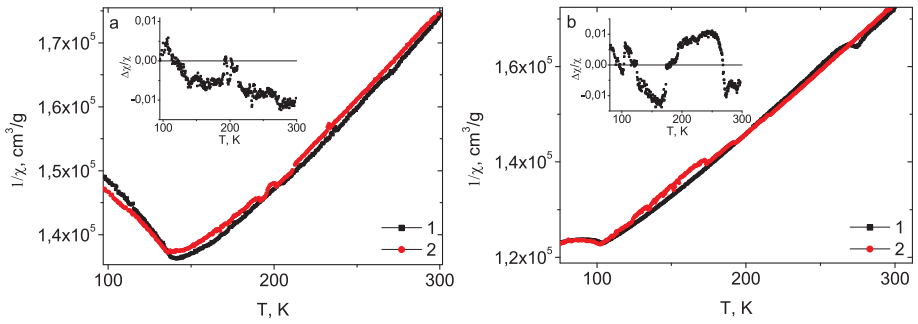

Fig. 11. Temperature dependence of inverse magnetic susceptibility 1/χ for the samples $Yb_xMn_{1-x}S$ with x = 0.05 (a), x = 0.15 (b) cooled without a field (1) and in a magnetic field H = 50 kOe (2). Insert: Temperature dependence of the difference in susceptibility of samples cooled without a field (ZC) and in a magnetic field (FC) $\Delta\chi/\chi = (\chi^{FC} - \chi^{ZC})/\chi^{ZC}$.

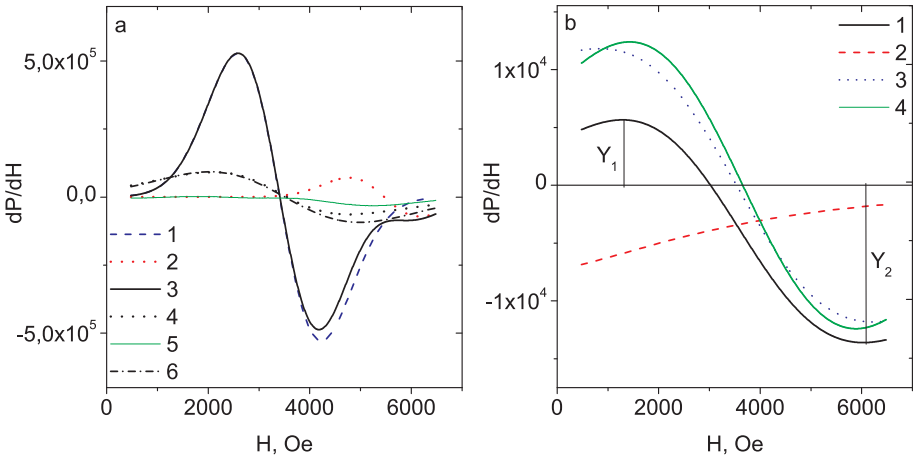

Fig. 12. Typical magnetic resonance spectrum in $Yb_{0.05}Mn_{0.95}S$ at T = 150 K (6), T = 280 K (3), lines 1, 2, 4, 5 – Lorentzian fitting lines, the solid line 3 represents the sum of the fitting curves 1,2; dotted line 6 represents the sum of the fitting curves 4,5; The experimental spectrum coincide with the sum of the fitting curves (a). The spectrum of $Yb_{0.15}Mn_{0.85}S$ at T = 180 K (1), T = 220 K (4), lines 2,3 – Lorentzian fitting lines, the solid line 1 represents the sum of the fitting curves sum peak (2,3) (b).

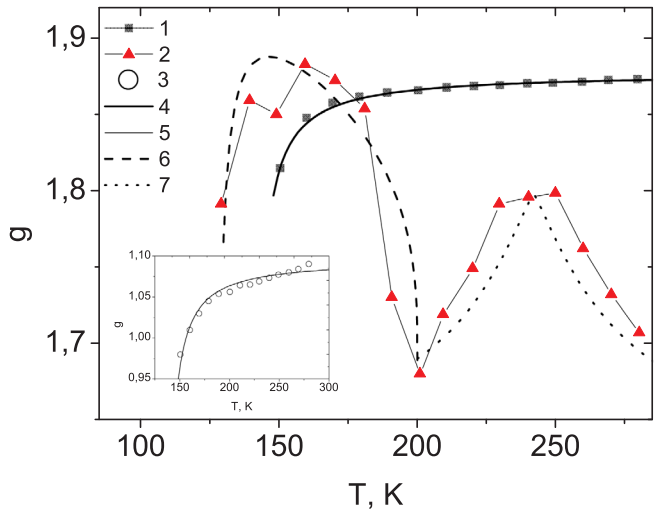

Fig. 13. Temperature dependence of g- factor of lines 1,4 (1) for the samples $Yb_{0.05}Mn_{0.95}S$ (1) and lines 3,4 (2) for $Yb_{0.15}Mn_{0.85}S$ (2). Insert: the temperature dependence of lines 2,5 of the EPR spectrum for x = 0.05. Fitting function for g-factor of lines 1,4 (4) (solid line) with parameters $H_{or}/H = 0.067$, b = 0.38 K, $\gamma = 1.1$ (4), for g- factor of lines 2,5 (5) with parameters $H_{or}/H = 0.048$, b = 2 K, $\gamma = 1.1$ in $Yb_{0.05}Mn_{0.95}S$ by Eq. (9) (solid line). For x = 0.15 fitting function for g- factor of lines 3,4 (6) (dotted line) by Eq. (10) with parameter $H_L = 0.34$, b = 0.7 K and fitting function (7) (point line) by Eq. (11) with parameters $H_{or}/H = 0.24$, A = −0.012 K, $\gamma = 1.2$, $\Delta T = 0.09$ K.

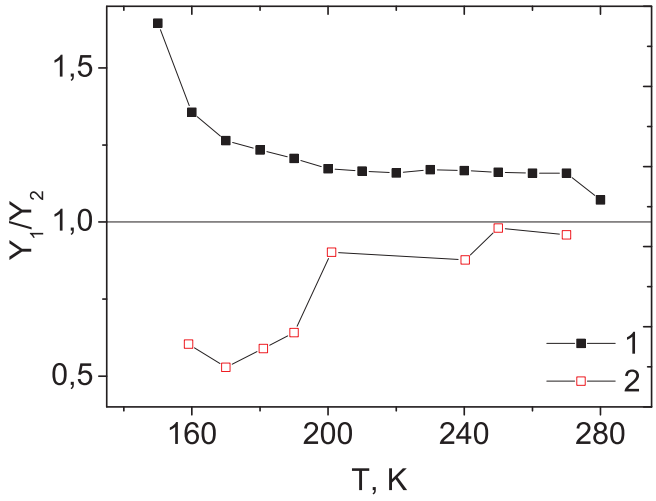

Fig. 15. Asymmetry of the EPR line shape for line 1,4 in $Yb_{0.05}Mn_{0.95}S$ (1) and for line 3,4 $Yb_{0.15}Mn_{0.85}S$ (2).

local regions with the orbital angular momentum form as a result of inter-center electron hoppings in the vicinity of ytterbium ions. Below 360 K, the angular momenta have a random direction $< L_i^z >_{in} \neq 0$ and the configuration mean over the lattice is $(\{\})\ \{ < L_i^z >_{in} \} = 0$. The orbital magnetic moments P_m for electrons and holes have different signs of $P_m = (e/m)\cdot L$. For holes, the directions of the orbital magnetic moment coincide with the spin direction, which leads to an increase in the magnetic susceptibility of the sample with x = 0.15 cooled in a magnetic field. The formation of octahedra with trigonal static distortion leads to uniaxial anisotropy with the Hamiltonian $H = g\mu_B \cdot HS + (DS^z)^2$, where $D = -\lambda^2/2E_{JT} = 0.8\ cm^{-1}$. This determines the splitting of the energy level of the ion spins in a zero external magnetic field and the appearance of an additional absorption line in the EPR for x = 0.15.

The EPR field consists of the sum of the fields: H is the external magnetic field, H_{or} is the field created by inter centered currents with

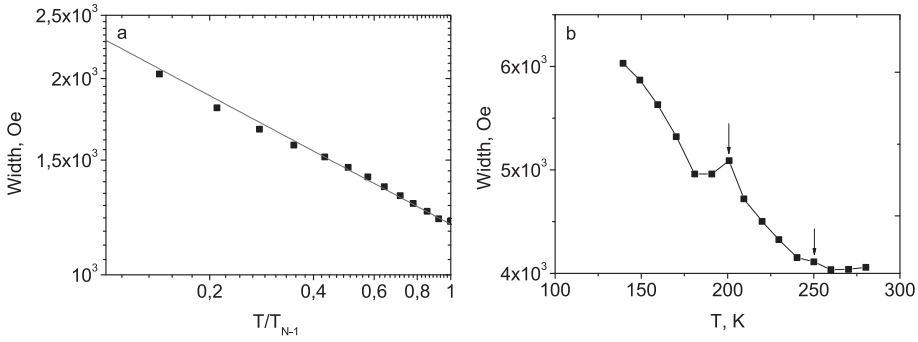

Fig. 14. Temperature dependences of EPR line width for line 1,4 sample $Yb_{0.05}Mn_{0.95}S$ in logarithmic coordinates (a) and for line 3,4 sample $Yb_{0.15}Mn_{0.85}S$ (b).

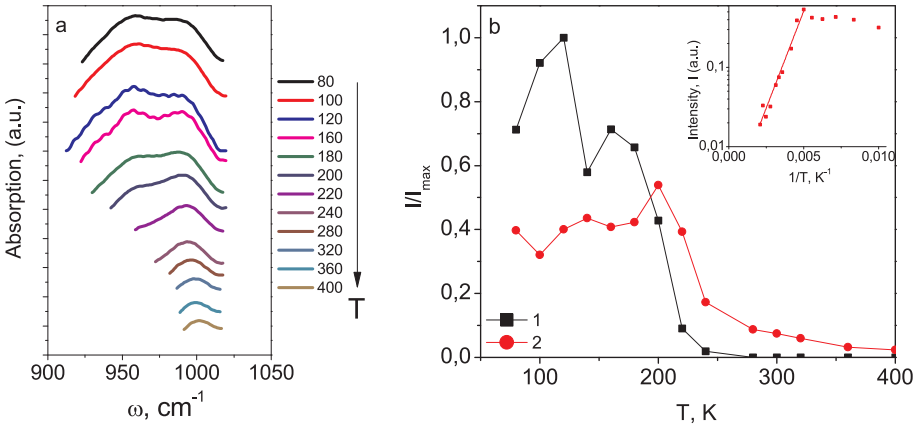

Fig. 16. IR absorption spectrum in the frequency range 900–1050 cm^{-1} for the sample $Yb_xMn_{1-x}S$ with x = 0.15 (a). (b) – Dependence of the normalized intensity on the temperature at the frequencies ω_1 (1) and ω_2 (2). Insert: Dependence of intensity of absorption peak at ω_2 on the inverse temperature 1/T for $Yb_xMn_{1-x}S$ with x = 0.15.

orbital momentum, the exchange field of the nearest neighbors is $H_{ex} = zJ \cdot M_{sub}$, z is the number of nearest neighbors, J is the exchange interaction, M_{sub} is the sublattice magnetization. In the molecular field approximation (MF), $M_{sub} = C \cdot H/T$, taking into account spin–spin correlations, $M_{sub} = \chi \cdot H = bH/(1–T/T_N)^{\gamma}$. The sublattice susceptibility χ diverges in the vicinity of the Neel temperature. Fitting function for g-factor:

$$g = \frac{2}{1 + \frac{H_{or}}{H} + \frac{b}{(T - T_N)^{\gamma}}} \quad (9)$$

well describes experimental data with two parameters $H_{or}/H = 0.067$, b = 0.38, $\gamma = 1.1$ для x = 0.05.

In the $Yb_{0.15}Mn_{0.85}S$ solid solution in the temperature behavior of g (T) we distinguish two regions of 100–200 K and 200–300 K. In the low-temperature region in g (T), one more contribution is added related to the ordering of the orbital magnetic moments into the site in a domain with the $L_s^z = L^z(0)\,(1–T/T_{JT})^{\beta}$ c $\beta = 0.31$, $T_{JT} = 200$ K. The function

$$g = \frac{0.75}{1 + H_L(1 - \frac{T}{T_{JT}})^{\beta}} + \frac{0.95}{1 + \frac{b}{(T - T_N)^{\gamma}}} \quad (10)$$

qualitatively describes the experimental results with $T_N = 126$ K, in the region of which the sublattice susceptibility sharply increases. The EPR line width increases sharply in the Fermi temperature range of the glass $T_F = 124$ K (Fig. 3), where $\Delta\chi/\chi = 0.6\%$ detects a jump (insert in Fig. 11). The dynamic JT transition at $T_{JT1} = 245$ K is associated with a change in type of the local vibrational modes from T_{2g} to T_{1g} at heating. The temperature dependence g-factor presents in the kind of:

$$g = \frac{2}{1 + \frac{H_{or}}{H} + \frac{A}{\left(abs\left(1 - \frac{T}{T_{JT1}}\right)^{\gamma} + \Delta T\right)}} \quad (11)$$

and describes experimental results with parameters $H_{or}/H = 0.24$, $\gamma = 1.2$ for x = 0.15 in the range of 200–300 K.

In the antiferromagnetic phase, at the random distribution of impurity electrons over the lattice sites, the spin-reorientation transition can occur upon heating if the effective magnetic field induced by the orbital magnetic moments $H_L = \lambda \cdot L^z$ satisfies the condition $H_L > H_{sf} = \sqrt{2H_eH_a}$, where H_e is the exchange field and H_a is the anisotropy field. At x = 0.05, this relation makes it possible to estimate the impedance jump temperature T = 125 K (insert in Fig. 5b) with parameters of $\lambda = 40$ cm^{-1}, $L^z = 0.1$ μ_B, $H_e = 160$ kOe, and $H_a = 6$ kOe and the sublattice magnetization of $M_s = 5\mu_B(1–T/T_N)^{1/2}$, which decreases according to the power law.

The magnetic field lifted threefold degeneracy of the orbital magnetic moment in the temperature range of distortion of octahedra with T_{1g} and T_{2g} types, which leads to high impedance values and to the dependence of the properties of $Yb_xMn_{1-x}S$ solid solutions on the prehistory. In the range of dynamic JT transitions, the relaxation time of current carriers sharply increases with hopping conduction involving phonons, because conductivity is directly proportional to the frequency and number of phonons.

7. Conclusions

The substitution of variable-valence ytterbium ions for manganese ions in the $Yb_xMn_{1-x}S$ system forms a nonuniform electron density distribution over the sample, which leads to the nonlinear *I–V* characteristics of the Poole–Frenkel type and the Mott law in the percolation concentration region. The temperature range of the Fermi formation of glass with a change in the type of conductivity from (1/T) to $(1/T)^{1/4}$ is found. Two dynamic JT transitions and a transition to stable static distortion of the octahedra from IR spectra and from the EPR spectra were established. The maxima of the mobility of current carriers in the region of these transitions and the energy barrier between the degenerate distortion directions of the octahedra are found. The trivalent state of the ytterbium ion and the asymmetry growth below 200 K were found from the EPR spectra and attributed to the growth of spin relaxation time as compared with spin diffusion. In the paramagnetic region upon cooling in a magnetic field the contribution of orbital magnetic moment to magnetic susceptibility was found. The dependence of the impedance on the sample prehistory in a magnetic field near Jahn-Teller transition was established. The functional dependence of relaxation of the charged particles and the critical frequency, above which the impedance is independent of temperature were determined.

CRediT authorship contribution statement

S.S. Aplesnin: Conceptualization, Writing - original draft. **M.N. Sitnikov:** Methodology, Investigation. **A.M. Kharkov:** Visualization, Writing - review & editing. **S.O. Konovalov:** Investigation. **A.M. Vorotinov:** Investigation.

Declaration of Competing Interest

The authors declare that they have no known competing financial interests or personal relationships that could have appeared to influence the work reported in this paper.

Acknowledgments

This study was supported by youth project_Reshetnev Siberian State University of Science and Technology.

References

[1] Y.J. Choi, C.L. Zhang, N. Lee, S.W. Cheong, Cross-control of magnetization and polarization by electric and magnetic fields with competing multiferroic and weak-

ferromagnetic phases, Phys. Rev. Lett. 105 (2010) 097201.
[2] S.S. Aplesnin, A.N. Masyugin, M.N. Sitnikov, U.I. Rybina, Takayuki Ishibashi, colossal magnetostriction and electrostriction of bismuth-substituted neodymium iron garnet films, J. Magn. Magn. Mater. 464 (2018) 44–49.
[3] D. Khomskii, Classifying multiferroics: mechanisms and effects, Physics 2 (2009) 20.
[4] S.S. Aplesnin, A.N. Masyugin, M.N. Sitnikov, T. Ishibashi, Effect of a substrate on the magnetoelectric effect in rare-earth-doped bismuth iron garnet, J. Exp. Theor. Phys. Lett. 110 (2019) 223–230.
[5] S. Farokhipoor, B. Noheda, Conduction through 71° Domain Walls in Thin Films, Phys. Rev. Lett. 107 (2011) 127601.
[6] C.J.M. Daumont, S. Farokhipoor, A. Ferri, J.C. Wojdeł, J. Iniguez, B.J. Kooi, B. Noheda, Tuning the atomic and domain structure of epitaxial films of multiferroic $BiFeO_3$, Phys. Rev. B 81 (2010) 144115.
[7] J. Seidel, P. Maksymovych, Y. Batra, A. Katan, S.-Y. Yang, Q. He, A.P. Baddorf, S.V. Kalinin, C.-H. Yang, J.-C. Yang, Y.-H. Chu, E.K. Salje, H. Wormeester, M. Salmeron, R. Ramesh, Domain wall conductivity in la-doped BiFeO, Phys. Rev. Lett. 105 (2010) 197603.
[8] Y.V. Pershin, M. Di Ventra, Experimental demonstration of associative memory with memristive neural networks, Neural Networks 23 (2010) 881–886.
[9] D.B. Strukov, G.S. Snider, D.R. Stewart, R.S. Williams, The missing memristor found, Nature 453 (2008) 80–83.
[10] W. Lu, S.H. Jo, T. Chang, I. Ebong, B.B. Bhadviya, P. Mazumder, Nanoscale memristor device as synapse in neuromorphic systems, Nano Lett. 10 (2010) 1297–1301.
[11] C.R. Wang, H.S. Kuan, S.T. Lin, Y.Y. Chen, The metal-insulator transition in Al-Pd-Re quasicrystals, J. Phys. Soc. Jpn. 67 (1998) 2383–2387.
[12] A. Schilling, R. Dell'Amore, J. Karpinski, Z. Bukowski, M. Medarde, E. Pomjakushina, K.A. Muller, $LaBaNiO_4$: a fermi glass, J. Phys. Condens. Matter 21 (2009) 015701.
[13] P. Strange, A. Svane, W.M. Temmerman, Z. Szotek, H. Winter, Understanding the valency of rare earths from first-principles theory, Nature 399 (1999) 756.
[14] L. Petit, A. Svane, Z. Szotek, P. Strange, H. Winter, W.M. Temmerman, Simple rules for determining valencies of f-electron systems, J. Phys. Condens. Matter 13 (2001) 8697–8706.
[15] K. Syassen, H. Winzen, H.G. Zimmer, H. Tups, J.M. Leger, Optical response of YbS and YbO at high pressures and the pressure-volume relation of YbS, Phys. Rev. B Condens. Matter 32 (1985) 8246–8252.
[16] C.M. Varma, Valence instabilities and related narrow band phenomena, Rev. Mod. Phys. 48 (1976) 219.
[17] M. Matsunami, H. Okamura, A. Ochiai, T. Nanba, Pressure tuning of an ionic insulator into a heavy electron metal: an infrared study of YbS, Phys. Rev. Lett. 103 (2009) 237202.
[18] P. Werner, E. Gull, M. Troyer, A.J. Millis, Spin freezing transition and non-Fermi-liquid self-energy in a three-orbital model, Phys. Rev. Lett. 101 (2008) 166405.
[19] S.S. Aplesnin, A.I. Moskvin, Effect of strong electron correlations and electron-lattice interaction on the ordering of electron orbitals, J. Exp. Theor. Phys. Lett. 92 (2010) 226–231.
[20] K.I. Kugel, D.I. Khomskii, The Jahn-Teller effect and magnetism: transition metal compounds, UFN 136 (1982) 621–664.
[21] R. Peters, N. Kawakami, T. Pruschke, Orbital order, metal-insulator transition, and magnetoresistance effect in the two-orbital Hubbard model, Phys. Rev. B 83 (2011) 125110.
[22] K.I. Kugel, A.L. Rakhmanov, A.O. Sboychakov, D.I. Khomskii, Doped orbitally ordered systems: another case of phase separation, Phys. Rev. B 78 (2008) 155113.
[23] S.S. Aplesnin, L.I. Ryabinkina, O.B. Romanova, V.V. Sokolov, A.Y. Pichugin, A.I. Galyas, O.F. Demidenko, G.I. Makovetski, K.I. Yanushkevich, Magnetic and electrical properties of cation-substituted sulfides $Me_xMn_{1-x}S$ Me = Co, Gd, Phys. Solid State 51 (2009) 698–701.
[24] R.H. Mitchell, Perovskites: Modern and Ancient, Journal of Applied Crystallography 58 (2002) 1075-1075.
[25] V.B. Shenoy, C.N.R. Rao, Electronic phase separation and other novel phenomena and properties exhibited by mixed-valent rare-earth manganites and related materials, Philos. Trans. R. Soc. A 366 (2008) 63–82.
[26] A. Moreo, S. Yunoki, E. Dagotto, Phase separation scenario for manganese oxides and related materials, Science 283 (1999) 2034–2040.
[27] G.A. Connell, D.L. Camphausen, W. Paul, Theory of Poole-Frenkel conduction in low-mobility semiconductors, Philos. Mag. 26 (1972) 541–551.
[28] B.I. Shklovsky, A.L. Efros, Electronic properties of doped semiconductors, Science, Moscow, 1979.
[29] H.H. Heikens, G.A. Wiegers, C.F. Bruggen, On the nature of a new phase transition in α-MnS, Solid State Commun. 24 (1977) 205.
[30] S.S. Aplesnin, L.I. Ryabinkina, G.A. Petrakovskii, G.M. Abramoba, N.I. Kiselev, O.B. Romanova, Influence of magnetic ordering on the resistivity anisotropy of α-MnS single crystal, Solid State Commun. 129 (2004) 195.
[31] V.V. Prudnikov, A.N. Vakilov, Computer modeling of the critical dynamics of dilute magnets, Lett. ZhETF 55 (1992) 709–712.
[32] V.V. Prudnikov, P.V. Prudnikov, A.S. Krinitsin, A.N. Vakilov, M.V. Rychkov, E.A. Pospelov, Short time dynamics and critical behavior of the three-dimensional site-diluted Ising model, Phys. Rev. E 81 (2010) 011130.
[33] H.Q. Heuer, Monte carlo simulation of strongly disordered Ising ferromagnets, Phys. Rev. B 42 (1990) 6476.
[34] N.Y. Wiley, Impedance spectroscopy: Emphasizing solid materials and Systems, by J. Ross Macdonald, 1988.
[35] E. Horwood, Instrumental methods in electrochemistry, Chichester, 1985.
[36] E.G. Batyev, Pauli paramagnetism and Landau diamagnetism, UFN 179 (2009) 1333–1334.
[37] R.M. White, Quantum Theory of Magnetism, Springer-Verlag, Berlin, Heidelberg, New York, 1983.
[38] S.A. Altshuller, B.M. Kozyrev, Elektronnyj paramagnitnyj rezonans soedinenij elementov promezhutochnyh grupp, Science, Moscow, 1972.
[39] L.M. Roth, g Factor and donor spin-lattice relaxation for electrons in germanium and silicon, Phys. Rev. 118 (1960) 1534–1540.
[40] J. Rodriguez-Carvajal, M. Hennion, F. Moussa, A.H. Moudden, L. Pinsard, A. Revcolevschi, Neutron-diffraction study of the Jahn-Teller transition in stoichiometric $LaMnO_3$, Phys. Rev. B 57 (1998) 3189.
[41] P. Novak, K.W.H. Stevens, The interaction between two T_{1g} (T_{2g}) Jahn-Teller ions, J. Phys. C Solid State Phys. 3 (2001) 1703.
[42] I. Leonov, D. Korotin, N. Binggeli, V.I. Anisimov, D. Vollhardt, Computation of correlation-induced atomic displacements and structural transformations in paramagnetic $KCuF_3$ and $LaMnO_3$, Phys. Rev. B 81 (2010) 075109.